Combined Experimental/Numerical Study on the Precipitation of Nanoparticles

Hans-Christoph Schwarzer
Institute of Particle Technology, Technische Universität München, 85748 Garching, Germany

Wolfgang Peukert
Institute of Particle Technology, Universität Erlangen-Nürnberg, 91058 Erlangen, Germany

DOI 10.1002/aic.10277
Published online in Wiley InterScience (www.interscience.wiley.com).

Nanoparticle precipitation in a T-mixer was investigated experimentally as well as through simulations based on the population balance equation coupled with a global mixing model using barium sulfate as the substance under investigation. A detailed predictive precipitation model is presented and the important model parameters are identified: the mixing kinetics, the interfacial energy, and the physicochemical calculation of supersaturation. Furthermore, the capability of the global mixing model was evaluated, achieving good agreement of the mean particle sizes between experimental and simulation results. Many insights into the kinetics and the relevant time scales of the competing steps such as micromixing (mixing at the molecular level), nucleation, growth, and aggregation are obtained. However, some discrepancies in the width of the particle size distributions remain that are attributed to spatial and temporal fluctuations in the flow field and, consequently, in the mixing kinetics that cannot be resolved by the applied global mixing model. © 2004 American Institute of Chemical Engineers *AIChE J,* 50: 3234–3247, 2004
Keywords: precipitation, micromixing, interfacial energy, population balance equation, nanoparticle, barium sulfate

Introduction

Precipitation is a widespread process in industry for the production of particles of various size distributions, morphologies, and other properties. To improve and predict the product properties of precipitation processes, as well as to apply precipitation to new products such as nanoparticles, further and deeper understanding of the involved steps is required. These product properties result from the competing kinetics of the various involved parallel and subsequent steps such as mixing, nucleation, growth, and secondary processes such as agglomeration, aggregation, or ripening. For the formation of nanoparticles, high levels of supersaturation—the thermodynamic driving force of phase transition—are necessary because of the highly nonlinear dependency of the nucleation rate on supersaturation. Consequently, because supersaturation is "generated" through micromixing (mixing on the molecular scale), fast mixing (high mixing intensities) is required (Schwarzer and Peukert, 2002, 2004). Furthermore, because of the small sizes and because particle formation is a very fast process (especially in nanoparticle precipitation), numerical methods have to be applied to elucidate important features of the process.

There are a number of studies on the effect of mixing in precipitation with different methods and objectives. However, micrometer-sized particles were formed in most studies. Torbacke and Rasmuson (2001) investigated mixing effects in a loop reactor; David (2001), Baldyga et al. (1995), and Phillips et al. (1999) used batch reactors with single or double feed. Couette-type precipitators were applied by Judat and Kind

Correspondence concerning this article should be addressed to W. Peukert at W.Peukert@lfg.uni-erlangen.de

(2002) and Barresi et al. (1999). Baldyga and Orciuch (2001) and Marchisio et al. (2002) used coaxial pipe reactors. Compared to static mixers such as T- and Y-mixers as well as other impinging jet reactors, the former reactors provide lower mixing intensities and (with the exception of the pipe reactors) the particles remain longer in a supersaturated environment, which leads to further growth. Thus they are not appropriate for the generation of nanoparticles.

Recent studies into nanoparticle precipitation, besides the work by the authors (Schwarzer and Peukert, 2002, 2004), were done by Heyer (2000), who investigated the formation of organic nanoparticles by drowning-out precipitation; by Eble (2000), who emphasized the significance of surface properties for precipitation kinetics and whose considerations are the basis of modeling the interfacial energy in this work; and by Schlomach et al. (2002), who studied the formation and aggregation of nanoparticles under shear stress.

Controlling and preventing particle aggregation is the further major task to be met in nanoparticle precipitation, given that particles can easily aggregate into the micrometer range within <1 s if no further measures such as electrostatic stabilization are taken. It is important that the stabilization kinetics is sufficiently fast. Using macromolecules for stabilization, this aspect might be critical. Electrostatic stabilization through the adsorption of potential determining ions on the particles' surfaces can be achieved by adding such ions to the suspension, preferably before precipitation, and by keeping the ionic strength as low as possible. For many salts, lattice ions can be considered as potential-determining ions because they fit perfectly onto the surface. For $BaSO_4$ nanoparticles the lattice ions as well as H^+ and OH^- ions can be considered potential determining (Eble, 2000). The adsorption isotherm of Ba^{2+} and H^+ ions on barium sulfate were determined by the authors (Schwarzer and Peukert, 2005).

Experimental

Precipitation experiments with barium sulfate as the model substance were carried out at 25°C as continuous experiments in a T-mixer, using aqueous solutions of barium chloride (VWR 101719, analytical grade) and sulfuric acid (VWR 109912, Combi-Titrisol) as feed solutions, forming barium sulfate according to Eq. 1. The T-mixer consists of two feed tubes of 0.5 mm diameter, positioned centrically opposite each other and the main tube with 1 mm diameter and 10 mm length. The relatively small geometric sizes of the mixer were chosen to provide intense mixing, necessary for nanoparticle precipitation. Nevertheless, the mixer capacity is remarkable: it is capable of mixing a total of 1 m^3 of aqueous solution within 24 h and thus precipitating about 100 kg of nanoscaled $BaSO_4$ if operated at a pressure drop of about 14 bar

$$BaCl_2 + H_2SO_4 \rightarrow BaSO_4 + 2HCl \qquad (1)$$

Constant pulsation-free flow rates for the (continuous) experiments are provided by a special device consisting of two pistons that are moved by a stepping motor and gear reduction in temperature-controlled tubes of high-precision DURAN® glass by Schott Geräte GmbH (Hofheim, Germany). Besides feed concentrations, the total flow rate was varied between 0.2 and 12 mL/s, using equivolumetric flow rates of the feeds. Thus the Re number, calculated based on the main tube diameter, varied between 250 and 15,000 and the mean residence time in the main tube between 0.67 and 40 ms. Samples were collected for analysis at steady-state operating conditions. The experimental setup is shown in Figure 1.

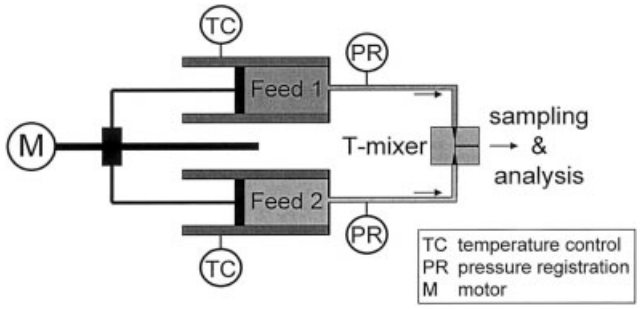

Figure 1. Experimental setup.

The obtained particle size distribution (PSD) was measured based on quasi-elastic light scattering using a commercial device (UPA 150 by Microtrac). The reproducibility of the experiments was checked and a standard deviation of the mean size of less than 7% was found based on 15 individual experiments. Additionally, after filtration and drying of the samples, the specific surface area was determined through nitrogen adsorption (BET), the morphology determined by X-ray diffraction and TEM, and AFM images taken to validate the measured sizes.

To quantify the mixing intensity, the pressure drop—important because it contains information on the total amount of friction and shear in the flow—was determined by recording the hydrostatic pressure upstream of the mixer (pressure sensor A08; Sensor-Technik Wiedemann) and applying the Bernoulli equation to calculate the pressure drop in the mixer. For that purpose, the pressure drop in the feed tubes between sensor and main tube was determined using a specially built adapter that included the 0.5-mm section of the mixer but not the main tube. A pressure drop coefficient referring to the mean velocity in the main tube of $\zeta = 12.56$, attributed to the mixing, was obtained (Eq. 2). Because the measured pressure drop did not change with increasing length of the main tube, it can be concluded that the pressure drop arises (almost) completely from the impinging of the two feeds

$$\Delta p = \frac{1}{2}\,\rho_F\,\zeta u_{mean}^2 \qquad (2)$$

Because of the mixer geometry (impinging of jets) and the resulting high pressure drop, the flow in the main tube can be considered turbulent for most of the investigated Re number range. This was confirmed by visualization experiments (which will by published) and by results by Telib et al. (2004), who used direct numerical simulation to calculate the flow field in a similar T-mixer configuration. They found a transition from periodic oscillating flow to turbulent flow in the range between $Re = 400$ and $Re = 500$.

From the measured pressure drop, the mean specific power input in the main tube can be calculated, and values ranging from about 10 W/kg ($Re = 250$) up to 2×10^6 W/kg ($Re =$

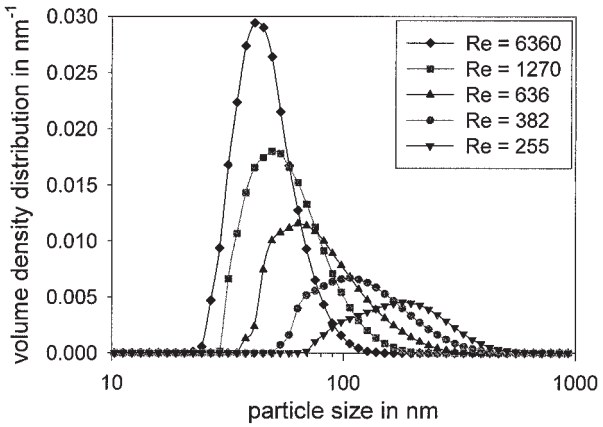

Figure 2. Measured particle size distributions of nanoscaled barium sulfate precipitated from 0.5 M $BaCl_2$ and 0.33 M H_2SO_4 solutions showing the influence of mixing intensity (Re number).

15,000) were obtained. The corresponding Kolmogoroff lengths are 18 μm and 840 nm, respectively, both well above the obtained particle sizes.

Figure 2 shows measured PSDs of barium sulfate nanoparticles precipitated from 0.5 M $BaCl_2$ and 0.33 M H_2SO_4 solutions at different flow rates. With increasing flow rate (Re number) and, consequently, increasing mixing intensity smaller particles are generated. This trend is confirmed by the TEM microphotographs shown in Figure 3 of barium sulfate precipitated from 0.7 M $BaCl_2$ and 0.23 M H_2SO_4 solutions at two different flow rates (Re = 382, left; Re = 6360, right). In these experiments a surplus of barium ions was chosen to electrostatically stabilize the generated suspensions against aggregation. For both sets of initial concentrations the generated suspensions can be considered stable within the timescale of interest: the increase of the volume-weighted mean particle size was measured to be <1 nm/min.

Precipitation Model

To deepen the understanding, to gain new insights, and to predict PSDs as steps toward predicting product properties, the precipitation process in the applied T-mixer is modeled and simulated, assuming plug flow through the mixer. Thus the model is one-dimensional (1D) spatially resolved. Based on this assumption, the evolution of the PSD with the position in the mixer is converted to a temporal evolution of the PSD. The particles in the model are characterized by the diameter x of the volume-equivalent sphere and the temporal evolution of the PSD is modeled based on the 1D population balance equation (Eq. 3), including the terms for nucleation, growth, and aggregation. To account for the mixing influence, the population balance equation is coupled by species balances with a mixing model, the *modified engulfment model of micromixing*, described as

$$\frac{\partial n(x)}{\partial t} = \underbrace{B_{hom}(S, \gamma_{CL})f[x_C(S, \gamma_{CL})]}_{\text{nucleation}} - \underbrace{\frac{\partial[G(S, x)n(x)]}{\partial x}}_{\text{growth}} + \underbrace{B_{agg}(n, x) - D_{agg}(n, x)}_{\text{aggregation}} \quad (3)$$

In this equation $n(x)$ is a number density concentration of particles of size x. The first term on the right-hand side accounts for nucleation, the second for growth, and B_{agg} and D_{agg} represent the aggregation process. The function $f(x_C)$ describes the number density distribution of the formed nuclei with x_C the size of the critical nucleus. Often, Dirac delta functions are used for $f(x_C)$. However, the delta function is not suitable in combination with the applied method of solution for the population balance equation. Additionally, it is likely that there are fluctuations of nuclei sizes even under constant conditions and, because for random fluctuations a Gaussian distribution is appropriate, a (narrow) Gaussian distribution is assumed for $f(x_C)$. To quantify the distribution width a standard deviation of 5% of the mean size is chosen. The influence of this choice was tested for standard deviations ranging up to 100% (larger values were not checked) without observing significantly different PSDs, thus confirming the applicability of the chosen function.

Supersaturation

The driving force for solid formation through nucleation and growth is supersaturation, a measure for the system's thermo-

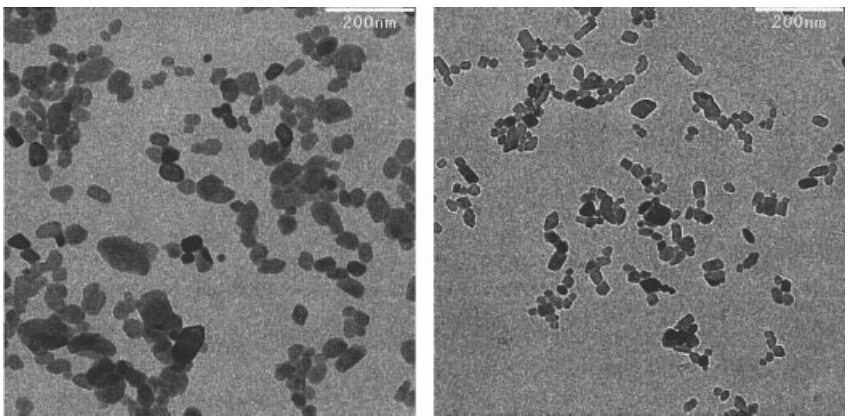

Figure 3. TEM micrographs of barium sulfate precipitated from 0.7 M $BaCl_2$ and 0.23 M H_2SO_4 solutions at Re = 382 (left) and Re = 6360 (right).

Table 1. Compilation of Values for the Solubility Product K_{SP} of Barium Sulfate at 25°C, Found in Literature

Source	Value of Solubility Product K_{SP}
Gmelin (1960)	1.08×10^{-10} (kmol^2/m^6)
Monnin and Galinier (1988)	8.91×10^{-11} (kmol^2/m^6)
Schubert (1998)	1.37×10^{-10} (kmol^2/m^6)
Monnin (1999)	9.82×10^{-11} (kmol^2/m^6)

dynamic offset from its equilibrium. For a binary salt such as barium sulfate, a concentration-based supersaturation S_c can be calculated from the ion concentrations and the solubility product K_{SP} as material property (Eq. 4). Various values of the solubility product, found in the literature, are compiled in Table 1. In this work, the value by Monnin (1999) is taken

$$S_c = \sqrt{\frac{c_{\mathrm{Ba}} c_{\mathrm{SO4}}}{K_{SP}}} \tag{4}$$

Under the investigated experimental conditions, however, additional factors have to be taken into account when calculating the real supersaturation: because of the high ionic strengths activities have to be used instead of concentrations, the incomplete dissociation of sulfuric acid has to be considered as well as the formation of metal–sulfate (ion-pair) complexes, as discussed in Monnin (1999).

The mean activity coefficient is calculated as a function of the ionic strength I and the concentrations of all electrolytes by the method proposed by Bromley (1973) as an advanced, multicomponent version of the Debye–Hückel limiting law, valid for ionic strengths up to 6 kmol m^{-3}. For the dissociation of sulfuric acid, the first stage can be considered complete and for the second stage a value of $K_{dis,2} = 1.2 \times 10^{-2}$ kmol m^{-3} at 25°C was taken from the literature (Gmelin Handbook, 1960). For the equilibrium constant for the formation of the barium sulfate ion-pair complex, a value of $K_{ip} = 1.91 \times 10^{-3}$ kmol/m^3 can be found in Felmy et al. (1990) and a value of $K_{ip} = 5.4 \times 10^{-3}$ kmol/m^3 can be found in Monnin (1999), both assuming that the activity coefficient for neutral species such as the ion-pair complex are close to unity. For consistency with the solubility product, the value by Monnin is used further on. It is important to emphasize that in this hybrid approach, the interaction of barium and sulfate ions in the solution are accounted for by the ion-pair complex and the interactions of these two ions with all other ions are accounted for by the activity coefficient.

To validate the approach, the solubility of barium sulfate in aqueous solutions of sodium sulfate is calculated and compared to experimental data by Jiang (1996) for three different model approaches: (1) concentration-based; (2) activity-based (that is, including the mean activity coefficient), without considering the formation of the ion-pair-complex; and (as most sophisticated model) (3) activity-based, including the formation of the ion-pair complex. The results are illustrated in Figure 4 and clearly show that the activity-based approach including the complex formation agrees best with the experimental data. The values of solubility product as well as the equilibrium constant of ion-pair formation at 20°C, corresponding to the temperature of the experimental data of Jiang (1996) (the experiments of this work were done at 25°C), were also taken from Monnin (1999).

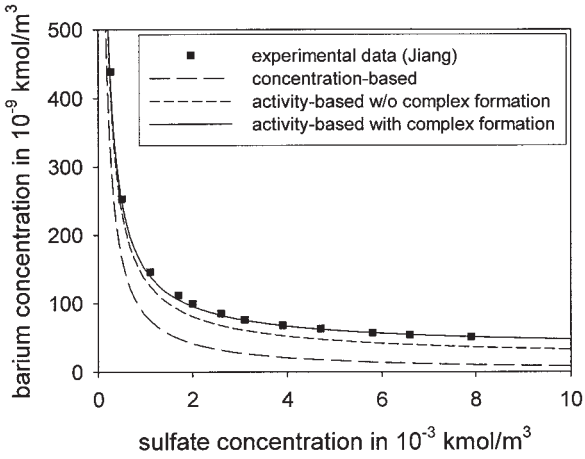

Figure 4. Solubility of $BaSO_4$ in aqueous Na_2SO_4 solutions (Comparison of experimental data by Jiang (1996) at 20°C with simulation results based on three different models).

The true Ba^{2+} and SO_4^{2-} concentrations and the mean activity coefficient are then calculated iteratively and used to calculate the real supersaturation S (Eq. 5). Table 2 shows a comparison of initial concentration-based and real supersaturations assuming instantaneous mixing. The deviation by a factor of 10 to 20 for the investigated feed concentrations clearly demonstrates that an enormous error would be made if concentration-based supersaturations would be used

$$S = \gamma_{\pm} \sqrt{\frac{c_{\mathrm{Ba},real}\, c_{\mathrm{SO4},real}}{K_{SP}}} \tag{5}$$

Nucleation

According to Mersmann et al. (2000), and supported by the experimental findings of Schubert (1998), primary homogeneous nucleation can be considered the dominant nucleation mechanism at the studied high supersaturations. The nucleation rate of homogeneous nucleation can be calculated based on the classical nucleation theory according to Eq. 6. Details on the derivation can be found in Mersmann (2000). The nucleation

Table 2. Comparison of the Initial Concentration-Based and Real Supersaturation for the Investigated Combination of Feed Concentration Assuming Instantaneous Mixing

$c_{\mathrm{BaCl2,Feed}}$	0.5 kmol/m^3	0.15 kmol/m^3	0.7 kmol/m^3	0.21 kmol/m^3
$c_{\mathrm{H2SO4,Feed}}$	0.33 kmol/m^3	0.1 kmol/m^3	0.23 kmol/m^3	0.07 kmol/m^3
S_c	20,495	6180	20,248	6118
S	1082	694	1076	682
Ratio S/S_c	0.053	0.112	0.053	0.111

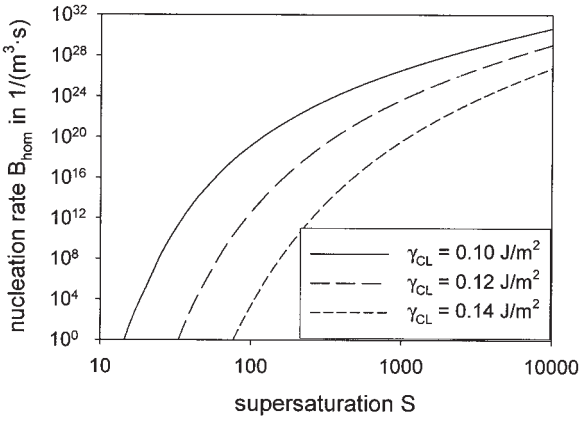

Figure 5. Homogeneous nucleation rates as function of supersaturation and interfacial energy calculated for barium sulfate.

rate strongly depends on supersaturation and on the interfacial energy γ_{CL} because the exponential term in the nucleation rate equation is a third-order function of the latter parameter. Figure 5 illustrates these dependencies for barium sulfate. The diffusion coefficient D_{AB} was calculated following the Stokes–Einstein relation and the molecular volume V_m was derived from the bulk density of barium sulfate (4500 kg/m^3). As can be seen from the illustration, an increase of the interfacial energy by 20% leads to a decrease of the nucleation rate by several orders of magnitude. Thus the interfacial energy is a critical parameter

$$B_{hom} = 1.5 D_{AB} (\sqrt{K_{SP}}\, S N_A)^{7/3} \sqrt{\frac{\gamma_{CL}}{kT}}\, V_m \times \exp\left(-\frac{16\pi}{3} \left(\frac{\gamma_{CL}}{kT}\right)^3 \frac{V_m^2}{(\nu \ln S)^2} \right) \quad (6)$$

Besides the nucleation rate, the size of the formed nuclei is also a function of both supersaturation and interfacial energy. To calculate the size x_C of the newly formed particles, the following equation for the critical nuclei size, taken from Mersmann (2000), is applied

$$x_C = \frac{4 \gamma_{CL} V_m}{\nu k T \ln S} \quad (7)$$

Growth

Particle growth, that is, the transport and integration of ions into the crystal structure of the particles, can be considered transport-controlled at high supersaturations (Mersmann et al., 2000). Angerhöfer (1994) experimentally determined the transition from integration- to transport-controlled growth at supersaturations of about $S = 40$, obtained for micrometer-sized particles in stirred batch experiments. For nanoparticles Eble (2000) derived an equation that can be used to estimate the size x of the particles at which the changeover from integration-controlled to transport-controlled growth takes places; states based on this equation (the changeover size for common sparingly soluble substances such as barium sulfate) is about ten times larger than the nucleus size corresponding to those conditions. Thus, assuming transport-controlled growth is applicable because the precipitated particles are much larger than the size of critical nuclei during most of the solid formation process.

The linear growth rate G (Eq. 8) is derived for spherical particles based on the mass transport equation stating that the mass flux equals mass transfer coefficient times surface area times activity gradient (that is, the difference of activities between bulk solution and the surface). The mass transfer coefficient is expressed through the Sherwood number (Sh) and the diffusion coefficient (D_{AB}), the latter calculated using the Stokes–Einstein equation. Because there is no relative motion between particles and surrounding fluid, Sh = 2 is assumed.

Because an excess of Ba^{2+} ions is used in the experiments (necessary for the electrostatic stabilization of the particles against aggregation), the activity gradient between bulk and surface is larger for Ba^{2+} ions than for SO_4^{2-} ions, resulting in a stronger diffusive transport of Ba^{2+} ions and leading to the buildup of charges on the surface. These charges electrostatically slow down the transport of further Ba^{2+} ions and enhance the transport of SO_4^{2-} ions toward the surface at the same time. Thus the transport is not a purely diffusional process but a combination of diffusion and electrostatic attraction/repulsion and the transport processes of both ion species interact through charging of the particle. As the surface charge builds up, differences between the transport rates of both species diminish and the rate of change of the surface charge decreases.

Because only few (excess) Ba^{2+} ions suffice for the buildup, a considerable surface charge compared to large amounts of (both) ions to form a particle, the buildup of surface charge can be considered much faster than the total duration of growth. Consequently, an "equilibrium" surface charge and pseudo-steady-state conditions are reached, characterized by equal transport rates of both ion species. Without equal transport rates in the pseudo-steady state, electroneutrality could not be kept both in the boundary layer and in the liquid phase far from the particle surface. Thus there is a mean transport rate that is larger than the transport rate of SO_4^{2-} ions and smaller than the rate of Ba^{2+} ions without considering the electrostatic influences. Because the activity gradients of both ion species vary during the process, so does the "equilibrium" surface charge.

In the derivation of Eq. 8, it is assumed that the "equilibrium" surface charge changes instantaneously. Furthermore, the activity gradient of the mean transport rate is approximated by the difference of the mean (geometric) activities between bulk and surface and, applying Eq. 5, the mean activities are expressed through the root of the solubility product times the supersaturation. At the surface equilibrium is assumed (that is, $S_{\text{surface}} = 1$)

$$G = \frac{\partial x}{\partial t} = 2 \frac{\mathrm{Sh}\, D_{AB} \sqrt{K_{SP}}\, M}{\rho_C} \frac{S - 1}{x} \quad (8)$$

Interfacial energy

The interfacial energy exhibits a strong influence on the nucleation rate (and consequently on the PSD) and it is thus a crucial parameter. Because changes in the interface imply an additional amount of work, the interface needs to be considered

in a thermodynamic description of the system. If the interface is charged (charge attributed to structure or structure defects of the particle as well as to adsorbed ions), the resulting electrical field also has to be considered.

Based on the concept of a *Gibbs dividing surface* and assuming constant temperature as well as equilibrium throughout the three-phase-system (solid, interface, liquid), the *Gibbs adsorption isotherm* (Eq. 9) can be derived analogously to the *Gibbs–Duhem equation* (Hunter, 1986; Sugimoto, 1996, 1999). In Eq. 9, Γ_i represents the surface concentration of component i in kmol/m^2 and $\mu_{i,el}$ represents the electrochemical potential of component i. For uncharged components, the electrochemical potential equals the chemical potential. Assuming Henry-type adsorption isotherms, the surface concentration Γ_i at adsorption equilibrium relates to the activities a_i of the adsorbing species in the solution according to Eq. 10

$$d\gamma = -\sum_i \Gamma_i d\mu_{i,el} \tag{9}$$

$$\Gamma_i = k_i a_i \tag{10}$$

The electrochemical potential can be divided into its chemical contribution μ_i (resulting from sorption) and its electrostatic contribution Ψ (approach of ions toward charged surface) (Eble, 2000; Hunter, 1986). Expressing the chemical potential through activities (Eq. 11) and also taking a possible structural surface charge density σ_0 into consideration, Eqs. 9, 10, and 11 lead to Eqs. 12 and 13

$$\mu_i = \mu_i^{\text{reference}} + RT \ln a_i \qquad d\mu_i = RTd(\ln a_i) \tag{11}$$

$$d\gamma = -\sum_i k_i a_i RTd(\ln a_i) - \sigma d\Psi \tag{12}$$

$$\sigma = \sigma_0 + \sum_i z_i F k_i a_i \tag{13}$$

Using the *Grahame equation* (Eq. 14) taken from Israelachvili (1991), which is based on the Boltzmann distribution of ions between a charged surface and the bulk at infinite distance, Eq. 12 can be integrated from the material-specific contribution γ_0, resulting in Eq. 15. The material-specific contribution γ_0 of the interfacial energy (that is, without considering adsorption) can be calculated by Eq. 16 (Mersmann, 1990), which is based on an observed correlation between interfacial energy and solubility (Nielsen and Söhnel, 1971). It is important to emphasize that the summation in the *Grahame equation* includes all ion species in the electrolyte

$$\sigma = \sqrt{2\varepsilon\varepsilon_0 kTN_A \sum_j \left\{ c_j \left[\exp\left(\frac{-z_j e\Psi}{kT}\right) - 1 \right] \right\}} \tag{14}$$

$$\gamma_{CL} = \gamma_0 - \underbrace{RT \sum_i k_i a_i}_{\text{chemical contribution}} - \underbrace{\int_0^{\Psi_0} \sigma(\Psi) d\Psi}_{\text{electrostatic contribution}} \tag{15}$$

$$\gamma_0 = 0.414kT \frac{1}{\sqrt[3]{V_m^2}} \ln\left(\frac{\rho_C}{M\sqrt{K_{SP}}}\right) \tag{16}$$

In summary, the interfacial energy of a solid–liquid interface at thermodynamic equilibrium depends through adsorption on the composition of the liquid phase. If the liquid phase contains adsorbing units, the interfacial energy is modified because of the adsorption (chemical contribution). If the adsorbing units are charged, an electrostatic contribution has to be considered additionally for work involved with the approach of ions through the electric field; in that case, ions that do not adsorb also influence the interfacial energy. Experimental evidence for such behavior is given, for example, by Butkus and Grasso (1998), who determined the interfacial energy of water/PTFE by contact angle measurements under variations of the sodium chloride concentration.

For the investigated system (barium sulfate precipitated from barium chloride and sulfuric acid aqueous solutions with an excess of barium ions), it is known by the work of Eble (2000) that only Ba^{2+} and H^+ ions adsorb significantly on barium sulfate particles. The adsorption isotherms of these two ions were determined quantitatively by the authors (Schwarzer and Peukert, 2005), based on the aggregation kinetics of nanoscaled barium sulfate suspensions and the stabilizing effect of adsorbed ions. The authors successfully applied Henry-type isotherms and obtained $k_{Ba} = 1.3 \times 10^{-8}$ m^3/m^2 as well as $k_H = 2.8 \times 10^{-9}$ m^3/m^2 as values of the adsorption (Henry) coefficients. Applying Eq. 16, a value of 0.1266 J/m^2 is obtained as material-specific contribution γ_0.

Aggregation and agglomeration

Aggregation (and agglomeration) is modeled (assuming binary aggregation) based on the work by von Smoluchowski (1917), distinguishing two reasons for collisions: collisions resulting from random Brownian motion, termed "perikinetic" or "Brownian"; and shear-induced collisions, termed "orthokinetic." For perikinetic aggregation, the collision rate can be calculated according to Eq. 17, whereas for shear-induced aggregation Eq. 18 is applied. The latter equation is based on the concept by Camp and Stein (1943), who were the first to apply the simple laminar shear-flow concept of von Smoluchowski to turbulent flows. Their concept was expanded by Saffman and Turner (1956) who took—besides velocity differences between particles—the relative velocity between particle and surrounding fluid into account

$$\beta_{coll,peri} = \frac{2kT}{3\nu_F \rho_F} (x_i + x_j)\left(\frac{1}{x_i} + \frac{1}{x_j}\right) \tag{17}$$

$$\beta_{coll,ortho} = \sqrt{\frac{\pi}{8 \times 15}} (x_i + x_j)^3 \sqrt{\frac{\varepsilon}{\nu_F}} \tag{18}$$

The Saffman and Turner approach to shear-induced collision rates assumes that the particles follow the fluid flow completely and that the particles are much smaller than the size of the smallest eddies of the turbulent flow, that is, smaller than the Kolmogorov length scale. For nanoparticles—that is, particles

with a characteristic length in the range of a few nanometers to several hundred nanometers—these limits are fulfilled.

An advanced method to calculate the collision rate in turbulent flows was presented by Kruis and Kusters (1997). This method is not limited to the above-mentioned restrictions concerning particle size and energy dissipation rate. However, it is far more complicated to calculate because detailed knowledge of several turbulence and flow field parameters is required that have to be obtained through computational fluid dynamics (CFD). For particles smaller than the Kolmogorov microscale the Saffman and Turner expression is to be preferred, as even Kruis and Kusters point out.

To decide whether the Brownian or the shear-induced collision mechanism dominates the aggregation of nanoparticles, the collision kernels are evaluated. At low energy dissipation rates ε, as in unstirred to moderately stirred suspensions, the aggregation of nanoparticles is dominated by the perikinetic mechanism. In highly turbulent flows such as the impinging zone of a T-mixer, however, orthokinetic (shear-induced) aggregation could dominate, especially for large particles. Because various regimes in terms of particle size and turbulence intensity are traversed during precipitation, it is necessary to consider both mechanisms.

Besides Brownian motion and turbulent shear as reasons for particle–particle collisions, the effect of particle–particle interactions on the number of collisions is included by a stability ratio W. This ratio describes the relative number of effective collisions without and with interactions in addition to omnipresent van der Waals forces. Such additional interactions, such as electrostatic forces, are attributed to the adsorption of ions on the particles and the resulting formation of an electrical double layer. Depending on the collision mechanism, there are different models to calculate the stability ratio W. For the Brownian mechanism, W is frequently calculated based on a transport approach by Fuchs (1934) on particle diffusion under the influence of particle–particle interaction, whereas for shear-induced collisions force-based approaches are to be preferred (Melis et al., 1999). Independent of collision mechanism, values for W are in the range of one to infinity. For the investigated system and purely Brownian collision mechanisms, the dependency of the stability ratio W on the composition of the solution was recently studied by the authors (Schwarzer and Peukert, 2005) and successfully correlated to the adsorption of Ba^{2+} and H^+ ions.

This leads to the following terms for the birth as well as the death rate density functions of the population balance equation

$$B_{agg}(n, x) = \frac{x^2}{2} \int_0^x \frac{\beta_{coll}(\sqrt[3]{x^3 - \lambda^3}, \lambda) n(\sqrt[3]{x^3 - \lambda^3}) n(\lambda)}{W(x^3 - \lambda^3)^{2/3}} \, d\lambda \qquad (19)$$

$$D_{agg}(n, x) = n(x) \int_0^\infty \frac{\beta_{coll}(x, \lambda)}{W} n(\lambda) d\lambda \qquad (20)$$

Mixing model

The relevant mixing process in precipitation is micromixing, that is, at length scales below the Kolmogorov scale down to molecular level. To account for the mixing influence, a modified model based on the *engulfment model of micromixing* by Baldyga and Bourne (1999) was previously derived (Schwarzer and Peukert, 2004) and coupled by species balances to the population balance equation.

The modified model is based on volume fractions X and assumes ideally mixed zones: one containing only feed solution A, one containing only feed solution B, and a contact zone. For simplification these zones are designated and indexed with A, B, and C for the contact zone. The contact zone itself consists of two zones, one zone containing only feed solution A, designated AC, and the mixing zone M containing both solutions. Thus $X_A + X_B + X_C = 1$ and $X_{AC} + X_M = X_C$. The model assumes that X_C increases when either A is mixed with B, A is mixed with C, or B is mixed with C. The mixing zone M increases as M is mixed either with B or with AC. To describe the mixing rates, second-order kinetic approaches are used and, as rate coefficient, the engulfment parameter E is used as in the Baldyga model. The resulting equations are given below. Concentrations in the mixing zone are then calculated by species balances, as follows

$$E = 0.058 \sqrt{\frac{\varepsilon}{\nu_F}} \qquad (21)$$

$$\frac{dX_C}{dt} = E(X_C X_A + X_C X_B + X_A X_B) \qquad (22)$$

$$\frac{dX_A}{dt} = -E\left(X_C X_A + X_A X_B \frac{X_A}{X_A + X_B}\right) \qquad (23)$$

$$\frac{dX_B}{dt} = -E\left(X_C X_B + X_A X_B \frac{X_B}{X_A + X_B}\right) \qquad (24)$$

$$\frac{dX_M}{dt} = E\left(X_C X_B + X_A X_B \frac{X_B}{X_A + X_B} + X_M(X_C - X_M)\right) \qquad (25)$$

As can be seen from Eq. 12 the engulfment parameter is a function of the specific power input ε and thus it (and consequently the mixing kinetics) depends on the profile of ε along the path through the mixer. In real mixers, however, the actual specific power input (that is, energy dissipation rate) fluctuates strongly with space and time. It is thus different for every infinite volume that flows through the mixer. Because real ε-profiles through the mixer are not known, four conservative, arbitrarily chosen profiles are evaluated, taking into consideration that the pressure drop arises mainly from the impinging:

- ε is constant through the mixer (termed *constant*)
- ε decreases with mixer length at a constant rate (*triangle*)
- 50% of the power input is dissipated within the first 10% (=1 mm) of the mixer (*step50*)
- 90% of the power input is dissipated within the first 10% (=1 mm) of the mixer (*step90*)

Using the presented profiles represents a good, global starting point to mixing modeling. Spatial and temporal resolution of mixing could, however, be necessary to capture the mixing more accurately.

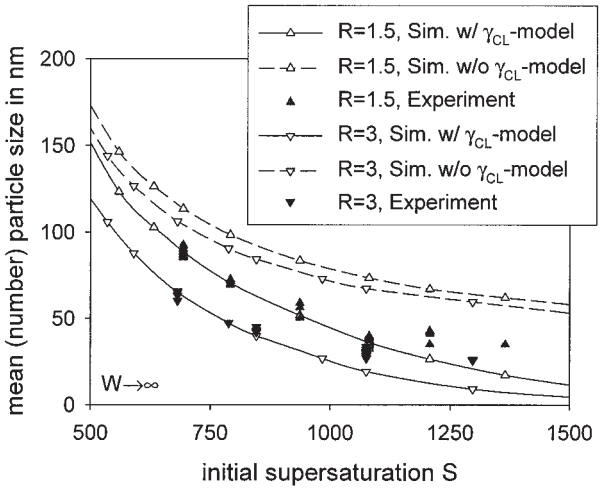

Figure 6. Comparison of experimental data obtained under presumably perfect mixing conditions and simulation results for instantaneous mixing showing importance of modeling the interfacial energy γ_{CL}.

Simulation Results

The precipitation process is simulated using the commercial software Parsival (CiT GmbH, Guben, Germany). The implemented algorithm uses a finite-element type Galerkin h-p method and applies a time discretization of Rothe's type. Besides computational speed, the main advantages of the Galerkin h-p method are that no assumptions concerning the shape of the PSD are necessary and that the overall accuracy can be estimated quantitatively from the mass defect during simulation. In the presented simulations, the mass defect was always within 0.7% of the theoretical value.

Perfect mixing

Figure 6 compares measured mean (number) particle sizes obtained under presumably perfect mixing conditions with simulation results, assuming instantaneous mixing with and without considering the changes in the interfacial energy attributed to composition based on the presented model. Based on the experimental findings it is believed that mixing in these experiments is fast enough (compare to Figure 7). Under these conditions the suspensions are sufficiently stabilized to neglect aggregation (Schwarzer and Peukert, 2005). The parameter R indicates the initial molar ratio of barium to sulfate ions, a parameter that was also varied.

As can be seen, the simulation results including the model of interfacial energy (solid lines) agree much better with experimental findings than those without considering the model (dashed lines), emphasizing the necessity to model the interfacial energy. The simulated (solid) lines including the model represent a lower limit for the particle size under the respective conditions (feed composition, temperature). Because of the competing kinetics of nucleation and growth, the minimal obtainable (mean) particle size (at perfect mixing) is limited by the feed concentrations. With higher concentrations, higher levels of supersaturation and, consequently, smaller particles are obtained; thus the limit is shifted toward smaller particles. Mixing effects, agglomeration, and aggregation would all result in larger particles.

The deviation for high supersaturations in Figure 6 between experiment and simulation could result from agglomeration or mixing, although based on the mixing model presented below mixing is sufficiently fast (deviation arises from the experiment). It could also be model-based because the γ_{CL} model is calculated from Henry-type adsorption isotherms with limited range of applicability and, consequently, with a tendency to underestimate the particle size with increasing supersaturation.

A further interesting aspect of this figure is that it shows the sensitivity of particle size on the interfacial energy in precipitation because, at $S = 1082$ and $R = 1.5$ for instance, a variation by less than 7% in the interfacial energy (from 0.1266 to 0.1181 J/m^2) more than doubles the resulting particle size under perfect mixing conditions. This clearly states the importance of knowing the interfacial energy at the corresponding thermodynamic equilibrium (at least under perfectly mixed conditions) as accurately as possible. In summary it can be said that the chosen model approach is capable of predicting mean particle sizes in nanoparticle precipitation under stable conditions and sufficiently fast mixing.

Influence of mixing

Figure 7 illustrates the influence of mixing on the PSD, represented by the number-weighted mean particle size. The results were calculated for the precipitation of $BaSO_4$ from 0.5 M $BaCl_2$ and 0.33 M H_2SO_4 solutions at 25°C and complete stabilization ($W \rightarrow \infty$). The interfacial energy was calculated based on the presented model only as function of the feed concentrations ($\gamma_{CL} = 0.1181$ J/m^2) without recalculating the value for each time step as a function of the actual composition. Different mixing conditions are expressed by the mean specific power input and the four chosen profiles of ε through the mixer were evaluated.

As can be seen in Figure 7 the calculated mean particle size decreases with mixing intensity for all four profiles from >200 to <40 nm. This is purely the result of the competing kinetics of nucleation and growth. At low supersaturations, far fewer

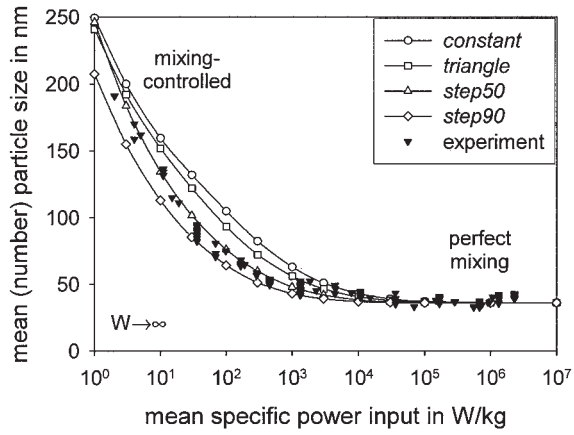

Figure 7. Influence of mixing on mean particle size and comparison of various ε-profiles, calculated for $BaSO_4$ precipitated from 0.5 M $BaCl_2$ and 0.33 M H_2SO_4 solutions at 25°C.

particles are nucleated than at higher supersaturations. These particles grow and thereby reduce supersaturation. Under the investigated conditions more than 99.9% of the supersaturation is reduced by growth.

Because the rates of nucleation and growth depend on supersaturation and thus the reduction rate of supersaturation (it increases with increasing supersaturation), the kinetics of solid formation results from the mixing kinetics unless mixing is much faster. Consequently, if the mixing kinetics is slow, lower levels of supersaturation are reached and fewer, but larger, particles are generated with the same total particle mass after precipitation. Figure 7 shows both cases: If mixing is as fast as or faster than the solid formation kinetics it has no influence on the resulting PSD. This limit is marked in Figure 7 as *perfect mixing*. The other case is designated as *mixing-controlled* because the mixing kinetics controls the solid formation kinetics and consequently the resulting PSD.

Figure 7 also compares the progression of particle size for the four chosen profiles of ε through the mixer, leading to differences in the mixing kinetics and consequently in the PSD. As can be seen, the experimental results agree best with the profile *step50*, that is, the profile that assumes that 50% of the power input is dissipated within the first 10% (1 mm) of the mixer. This profile probably accounts best for the average spatial and temporal distribution of ε in the mixer from among the four profiles because the power input arises from the impinging of the jets within the first section of the mixer main tube.

It is important to emphasize that all profiles were chosen without detailed knowledge on the flow field in the mixer and that applying CFD would give much more realistic profiles. The presented model based on the global approach to mixing, however, is much less time intense and was chosen to evaluate its potential and limits as well as to identify crucial parameters. Compared to the global approach, a CFD-based approach, however, would involve much more computational effort.

Influence of interfacial energy

In the simulation results shown so far, the interfacial energy is calculated for each set of feed concentrations based on the thermodynamic equilibrium of the composition after precipitation. This (although improved) treatment of the interfacial energy can still be considered an approximation because the interfacial energy might vary during the process as a result of changes in composition by the progress of mixing (but not by solid formation, given that the kinetics of solid formation do not change the thermodynamic equilibrium of the system). The resulting effect was also simulated by recalculating the interfacial energy for each time step as function of the liquid phase composition. To distinguish both treatments of the interfacial energy, the former is designated "without recalculation" and latter "with recalculation" in the following. Both treatments should, of course, give the same results for sufficiently fast mixing.

The results are depicted in Figure 8 which compares experimental data with simulation results for the precipitation of $BaSO_4$, using the *step50* profile for the mixing model and assuming complete stabilization ($W \rightarrow \infty$) in the simulations. Without considering the influence of composition at all (squares), the mean particles sizes are clearly overestimated, as

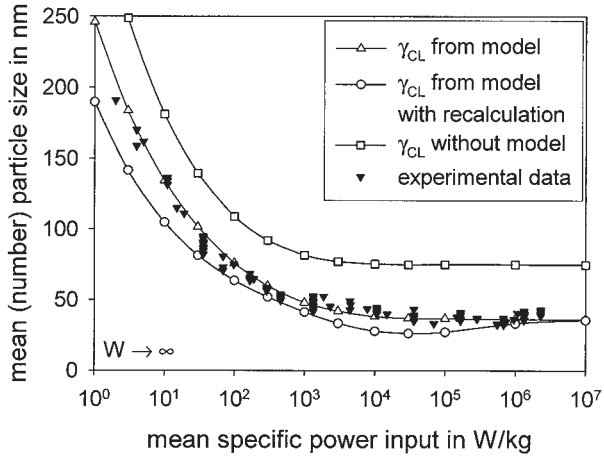

Figure 8. Comparison of experimental data and simulation results with and without considering changes of the interfacial energy arising from composition and mixing, calculated for $BaSO_4$ precipitated from 0.5 M $BaCl_2$ and 0.33 M H_2SO_4 solutions at 25°C.

was already shown in Figure 6. The two other plots with open symbols in Figure 8 are simulation results including the model of the interfacial energy without (triangles) and with recalculation (diamonds). For high values of epsilon (fast mixing), no significant difference in the particle size is observed, as expected (necessary condition). For smaller values of epsilon the simulated mean sizes including recalculation are smaller than those without the recalculation of the interfacial energy for each time step. This arises from the fact that the calculated interfacial energies of both feed solutions are, because of larger ion concentrations at the corresponding equilibria, smaller than those in the perfectly mixed solution. For these lower concentrations, the simulated sizes with and without recalculation differ less. No significant difference in the shape/width of the PSD was found between the interfacial energy models with and without recalculation.

A critical aspect of the model with recalculation is the uncertainty concerning its accuracy because the interfacial energies of the feed solutions were calculated based on extrapolating the Henry-type adsorption isotherms for Ba^{2+} and H^+ ions, which were determined under solution compositions similar to those of the mixed solution (Schwarzer and Peukert, 2005). For higher ion concentrations, the ion adsorption could be overestimated (maybe even substantially) and thus the interfacial energy and consequently the particle size would be underestimated. Unfortunately, the range of applicability of the adsorption isotherms is not clear. Also the minimum at a mean specific power input of about 10^4 W/kg in the simulated plot including recalculation in Figure 8 is not observed in the experimental data (perhaps because of the experimental accuracy).

Furthermore, it might seem surprising that the differences in mean particle size attributed to the interfacial energy models are relatively small, smaller than the differences arising from the different mixing kinetics (epsilon profiles) shown in Figure 7 (the real ε-profile through the mixer is unknown). Based on the sensitivity of the nucleation rate on interfacial energy and

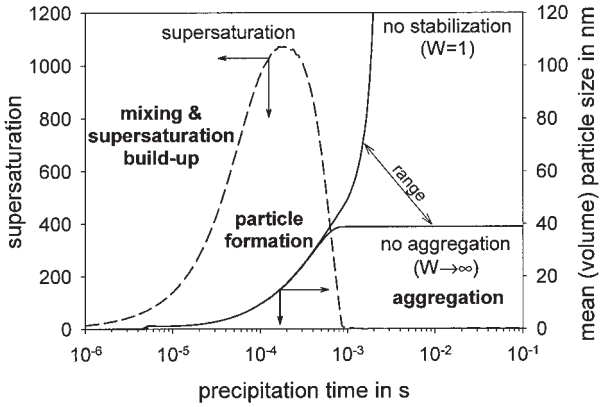

Figure 9. Temporal evolution of supersaturation and mean particle size during precipitation calculated for $BaSO_4$ precipitated from 0.5 M $BaCl_2$ and 0.33 M H_2SO_4 solutions at 25°C using a mean specific power input of 3×10^4 W/kg in combination with the *step50*-profile to describe the mixing rate.

because the latter varies by about 10% during mixing under these conditions (the difference between γ_{CL} without model and the model without recalculation is only 7% and a large deviation can be seen in Figure 8), one would expect a much larger influence. However, because of the dependency of the nucleation rate on supersaturation, most particles nucleate at maximum supersaturation, which does not occur until a large degree of mixing has taken place. Thus as most nuclei are formed, the value of the interfacial energy is already close to the value at *perfect mixing* and, consequently, the differences in mean particle size are relatively small.

Because the approach including recalculation depends on the mixing kinetics and consequently on the chosen epsilon profile through the mixer and, because its accuracy is uncertain, the approach without recalculation seems preferable and it appears more worthwhile to improve the model of the mixing influence.

Time scales in precipitation

Figure 9 shows the evolution of supersaturation and volume-weighted mean particle size with time for $BaSO_4$ precipitated from 0.5 M $BaCl_2$ and 0.33 M H_2SO_4 solutions at 25°C. The interfacial energy was calculated based on the model without recalculation (γ_{CL} = 0.1181 J/m^2). To quantify mixing, a specific power input typical for good mixing in the applied T-mixer ($\varepsilon_{mean} = 3 \times 10^4$ W/kg) in combination with the *step50*-profile was used.

After about 1 μs supersaturation buildup through mixing starts. As the supersaturation increases, the nucleation rate increases and at about 10 μs, the first particles occur as a result of nucleation (amount larger than numeric tolerance). These particles then grow and further nuclei are simultaneously generated. The evolution of supersaturation is still dominated by the buildup through mixing, although the reduction of supersaturation resulting from solid formation (nucleation and growth) continuously increases. At about 0.2 ms, supersaturation buildup and supersaturation reduction are equal. Afterward, the evolution of supersaturation is dominated by the solid formation and mixing becomes complete. After about 1 ms, the whole precipitation process is complete, that is, the supersaturation is reduced to saturation and the primary particles are formed. Secondary processes such as aggregation could now dominate changes in the PSD. The potential influence of aggregation considering both the Brownian and the turbulent mechanisms, ranging between maximal aggregation (that is, no stabilization, $W = 1$) and complete stabilization ($W \rightarrow \infty$), is also shown in Figure 9. Because the timescales in precipitation are very short, measuring the temporal evolution of PSD remains a challenge.

Impact of agglomeration and aggregation

To evaluate the effect of aggregation, simulations including both shear-induced and Brownian aggregation were performed. If the particles aggregate before supersaturation is completely reduced to saturation (that is, during solid formation), strong material bridges between the particles could be formed through growth, making redispersion impossible. Because of the possible formation of these strong chemical bonds between the particles, aggregation during solid formation is called *agglomeration* in the following.

For shear-induced agglomeration, the total impact on the PSD during solid formation depends on two parameters: the collision rate, which depends on the degree of turbulence; and the duration of solid formation, that is, the time it takes to completely reduce supersaturation to saturation. For the precipitation of $BaSO_4$ it was concluded that the strongest impact occurs at highest power inputs because under such conditions mixing can be considered instantaneous and the kinetics of solid formation is not accelerated with increasing power input in contrast to the collision rate. Thus simulations from 0.5 M $BaCl_2$ and 0.33 M H_2SO_4 solutions at 25°C, including shear-induced aggregation using a mean specific power input of 10^7 W/kg in combination with the *step50*-profile for the mixing model were performed without considering that the degree of turbulence might decrease significantly toward the mixer end and that it is substantially reduced as the suspension leaves the mixer. Thus the simulated impact of shear-induced aggregation

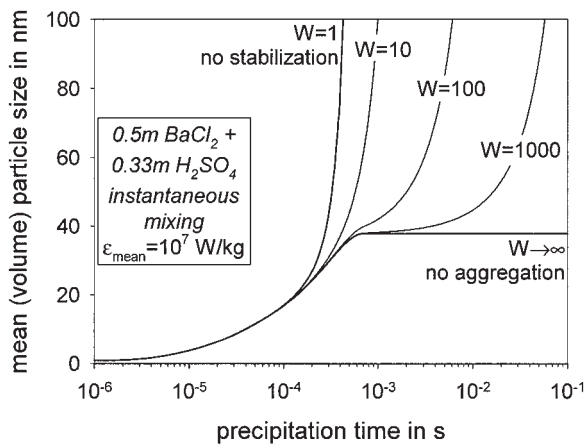

Figure 10. Impact of shear-induced aggregation on mean particle size during and after solid formation at various stability conditions.

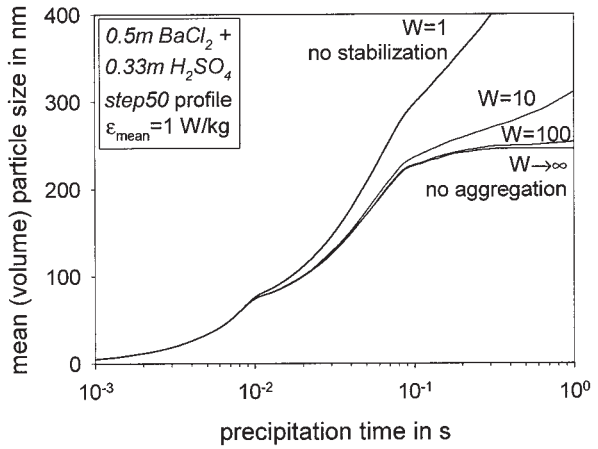

Figure 11. Impact of Brownian aggregation on mean particle size during and after solid formation at various stability conditions.

is overestimated. Again, the interfacial energy was calculated based on the model without recalculation ($\gamma_{CL} = 0.1181$ J/m^2).

The results, plotted in Figure 10, show the temporal evolution of the mean particle size for various stability conditions ranging from no stabilization ($W = 1$) to complete stabilization ($W \rightarrow \infty$). As can be seen, only if there is no stabilization, shear-induced agglomeration occurs significantly during solid formation. Even at weak stabilization ($W > 10$–100), solid formation is complete before the effect of agglomeration becomes significant. For lower values of the mean specific power input, less impact of shear-induced agglomeration was found, which can be attributed to the reduced number of collisions attributed to both, the collision rate (Eq. 18) and the smaller number densities $n(x)$ attributed to mixing: the size of primary particles increases and thus the total number of particles decreases with decreasing mixing intensity.

By a closer look at the involved timescales it becomes clear that the stabilization has to occur within less than milliseconds to prevent shear-induced agglomeration (and aggregation). This might be critical if macromolecules are used for stabilization. On the other hand, electrostatic stabilization through potential determining ions is feasible because ion adsorption kinetics and growth kinetics are correlated, especially if the adsorbing ions also contribute to growth as in the investigated case (Ba^{2+} ions). It also becomes clear that whether potential determining ions or macromolecules are used for stabilization, they have to be added to the suspension before mixing and solid formation because, otherwise, they would have to be added, mixed perfectly at molecular level, and provided enough time for adsorption, all within <1 ms after the initiation of precipitation.

Another possibility of preventing shear-induced agglomeration is to optimize the flow field (that is, to reduce the degree of turbulence after mixing is complete), such as by adapting the residence time in a static mixer by the mixer length in such manner that mixing is just complete at the end of the mixer, or by tailoring the mixer geometry. Then, instead of in highly turbulent flows, solid formation takes place in a slightly moving, perfectly mixed suspension and thus shear-induced agglomeration is reduced, or even prevented, by the mixer design.

For Brownian agglomeration, the strongest impact occurs at the slowest solid formation, that is, at the slowest mixing conditions. This case was investigated by simulating the precipitation of $BaSO_4$ from 0.5 M $BaCl_2$ and 0.33 M H_2SO_4 solutions including Brownian aggregation using a mean specific power input of 1 W/kg in combination with the *step50*-profile for the mixing model. Again, the interfacial energy was calculated based on the model without recalculation ($\gamma_{CL} = 0.1181$ J/m^2). Figure 11 shows, similar to the results of shear-induced aggregation, that Brownian agglomeration occurs significantly only if there is no stabilization. Even at weak stabilization ($W \geq 10$), solid formation is complete before the effect of agglomeration becomes significant. Thus Brownian agglomeration during solid formation and, consequently, the formation of material bridges between particles can also be avoided even by weak stabilization.

After solid formation and without stabilization, both mechanisms would—within seconds—lead to particles with sizes well in the micrometer range, as indicated in Figures 10 and 11. Thus again sufficient stabilization is necessary to obtain nanoparticle suspensions. Details on the stability of nanoscaled barium sulfate suspensions after solid formation can be found in a previous study by the authors that quantified the stability ratio W after solid formation (Schwarzer and Peukert, 2005), based on measured aggregation kinetics. For the compositions of this study, the values of the stability ratio are sufficiently large.

However, there are no data on the stability ratio during solid formation. To estimate the maximal possible impact of Brownian and shear-induced agglomeration, simulations based on the previous composition, the *step50*-profile for mixing and shear-induced aggregation and the interfacial energy calculated without recalculation were performed assuming that the stability ratio $W = 1$ during solid formation until 99% of the mass is transferred. Afterward complete stabilization is assumed. Additionally it is assumed that shear-induced agglomeration occurs only during the mean residence time of the mixer to take the effect of the mixer geometry into account. The results are plotted in Figure 12 and show the dominance of the Brownian mechanism at slow mixing and the dominance of the turbulent mixing at intense mixing. The maximum arises according to

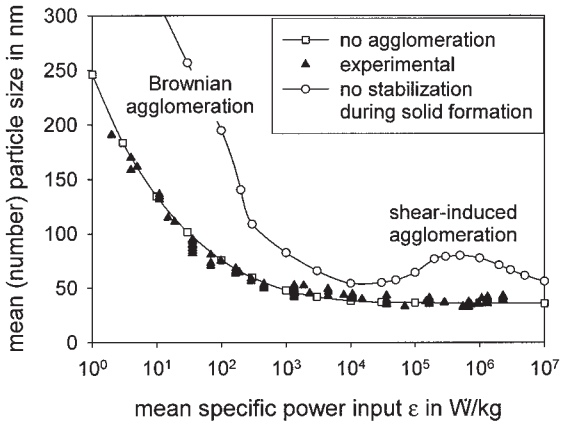

Figure 12. Simulated maximal impact of agglomeration (that is, aggregation during solid formation) and comparison to experimental data.

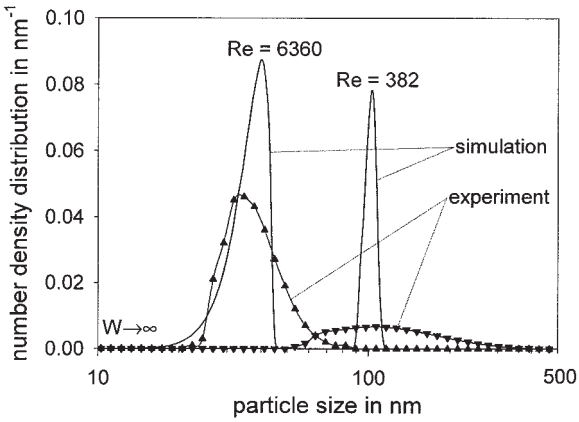

Figure 13. Comparison of PSDs obtained from experiment and simulation for the precipitation of $BaSO_4$ at Re = 6360 and Re = 382 in a T-mixer.

the residence time effect: for larger specific power inputs, the residence time in the mixer is shorter than the solid formation time and thus shear-induced agglomeration stops (according to the chosen stability conditions) before solid formation is complete. Concerning the stabilization against agglomeration, for the investigated set of feed concentrations it appears to be sufficient, even during solid formation.

Comparing the temporal evolution of particle size in Figures 9, 10, and 11 further insights into the dependency of particle size as well as solid formation time on mixing conditions can be gained: Within the investigated range of mixing conditions, the solid formation time using the same feed solutions was found to vary by about three orders of magnitude.

Comparison of particle size distributions

Figure 13 compares measured PSDs with simulation results as number density distributions for the precipitation of $BaSO_4$ from 0.5 M $BaCl_2$ and 0.33 M H_2SO_4 solutions at two Reynolds numbers (that is, mixing conditions), in combination with the *step50*-profile for the mixing model, considering the interfacial energy calculated without recalculation and assuming complete stabilization. Both distributions agree to some extent, although the simulated distributions underestimate the width, especially for large particles.

This discrepancy between experiment and simulation is attributed to the assumption of plug flow through the mixer. Resolving the flow field with space and time would lead to a broader spectrum of mixing conditions (many ε-profiles instead of one ε-profile) and consequently to broader distributions. Furthermore, possible longer residence times of the particles in a supersaturated environment attributed to back-flow zones and large eddies (neglected in the presented model by the assumption of plug flow through the mixer) would also be considered, leading to the formation of a greater number of larger particles in the simulation than in the current model. Although it is not clear at the moment whether these effects would account for all differences in the PSDs or only diminish the differences to some extent, based on the data shown in Figure 7 on the influence of the ε-profiles, a significant increase in the simulated width can be expected. Thus using CFD to calculate the flow field in the mixer in combination with Lagrangian particle tracking and a coupling with the population balance seem worthwhile and is currently under investigation. Through the coupling the whole process including mixing can be studied in greater detail and more realistic PSDs can be predicted.

Conclusions

Nanoparticle precipitation was investigated experimentally as well as through simulations using barium sulfate as the investigated material. A precipitation model based on the population balance equation and coupled with a global mixing model was presented and tested. A special feature of the precipitation model is that all its kinetic parameters can be derived from material properties, such as solubility and density, and thus the model can be considered predictive. As important parameters in the modeling of nanoparticle precipitation, the physicochemical aspects in the calculation of supersaturation, calculating the interfacial energy as a function of composition, and an appropriate modeling of the mixing kinetics are identified.

Good agreement in mean particle size between experiment and simulation is obtained if the interfacial energy is calculated based on the presented approach. The coupling with the global mixing model was found to work successfully with respect to mean sizes, although it involves some uncertainties concerning the distribution of the specific power input in the mixer. Many insights into the process and the involved timescales of solid formation are obtained, ranging (for complete solid formation) from less than milliseconds at intense mixing up to hundreds of milliseconds at slow mixing. Because the rates of nucleation and growth depend on supersaturation, a minimal particle size limit was identified as a function of feed composition, which represents perfect mixing and complete stabilization.

Agglomeration was investigated considering both shear-induced and Brownian aggregations. It was found that Brownian agglomeration dominates at slow mixing conditions and shear-induced aggregation dominates at fast mixing. Thus both mechanisms have to be considered in the model. Concerning the stability, it was calculated that even at weak stabilization no significant impact on particle size occurs during solid formation. However, without stabilization, the impact is significant and an estimate of the maximal impact was calculated. For the investigated set of feed concentrations, however, the stability appears to be sufficient even during solid formation. Nevertheless, stabilization is necessary because, otherwise, the particles would aggregate within seconds into the micrometer range.

A comparison of PSDs showed that the width of the PSD is underestimated in the simulations. Based on the detected strong influence of the chosen mixing histories this is attributed to the assumptions of plug flow and the neglect of considering spatial and temporal fluctuations in the approach. Resolving the flow field with space and time would lead to a broader spectrum of mixing conditions and, consequently, to broader distributions. Possible longer residence times in a supersaturated environment attributed to back-flow zones and large eddies (neglected in the global model by the assumption of plug flow through the mixer) would lead to the formation of more and larger particles in the simulation than in the current model. Thus a significant increase in the simulated width can be expected if the spectrum

of mixing conditions is included in the model. Nevertheless, the presented model represents an appropriate and now-validated approach to the predictive simulation of mean particle sizes in nanoparticle precipitation.

Notation

a_i = molar activity of species i, kmol m^{-3}
B_{agg} = birth rate density function of aggregation, m^{-4} s^{-1}
B_{hom} = nucleation rate, m^{-3} s^{-1}
c = molar concentration, kmol m^{-3}
D_{AB} = diffusion coefficient, m^2 s^{-1}
D_{agg} = death rate density function of aggregation, m^{-4} s^{-1}
e = elementary electric charge (1.602×10^{-19}), C
E = engulfment parameter, s^{-1}
F = Faraday constant (9.6485×10^7), C kmol^{-1}
$f(x_C)$ = function describing the density distribution of nuclei
G = linear growth rate, m s^{-1}
I = ionic strength, kmol m^{-3}
k_i = adsorption coefficient of species i, m^3 m^{-2}
k = Boltzmann constant (1.381×10^{-23}), J K^{-1}
K_{dis},2 = second stage dissociation constant of sulfuric acid, kmol m^{-3}
K_{ip} = equilibrium constant of ion-pair complex formation, kmol m^{-3}
K_{SP} = solubility product, kmol^2 m^{-6}
M = molecular weight, kg kmol^{-1}
N_A = Avogadro's number (6.023×10^{26}), kmol^{-1}
$N(x)$ = particle number density of size x, m^{-4}
R = initial molar ratio of barium to sulfate ions
R = ideal gas constant (8314), J kmol^{-1} K^{-1}
Re = Reynolds number
S = supersaturation
S_c = concentration-based supersaturation
Sh = Sherwood number
T = temperature, K
t = time, s
u_{mean} = mean velocity in the main tube of mixer, m s^{-1}
V_m = molecular volume, m^3
W = stability ratio
X, $x_{i,\,xj}$ = volume-equivalent particle diameter, m
x_c = size of a critical nucleus, m
X_i = volume fraction of zone i
z_i = ion valency of species i

Greek letters

β_{coll} = particle–particle collision rate, m^3 s^{-1}
Δp = pressure drop, Pa
Γ_i = surface concentration of species i, kmol m^{-2}
γ, γ_0, γ_{CL} = interfacial energy, J m^{-2}
$\gamma_\pm$ = activity coefficient
ε = relative permittivity
ε = electric field constant (8.854×10^{12}), C^2 J^{-1} m^{-1}
ε = specific power input (that is, energy dissipation rate), W kg^{-1}
ζ = pressure drop coefficient
λ = integration parameter (volume-equivalent particle diameter), m
μ_i = (electro-)chemical potential of species i, J
ν = dissociation number
ν_F = kinematic viscosity of fluid, m^2 s^{-1}
ρ_C = density of particles, kg m^{-3}
ρ_F = density of fluid, kg m^{-3}
σ, σ_0 = surface charge density, structural surface charge density, C m^{-2}
Ψ, Ψ_0 = electrical potential, surface potential, V

Literature Cited

Angerhöfer, M., "Untersuchung zur Kinetik der Fällungskristallisation von Bariumsulfat," PhD Thesis, Technische Universität München, Germany (1994).

Baldyga, J., and J. R. Bourne, *Turbulent Mixing and Chemical Reactions*, Wiley, Chichester, UK (1999).

Baldyga, J., and W. Orciuch, "Barium Sulfate Precipitation in a Pipe—An Experimental Study and CFD Modeling," *Chem. Eng. Sci.*, **56**, 2435 (2001).

Baldyga, J., W. Podgorska, and R. Pohorecki, "Mixing-Precipitation Model with Application to Double Feed Semibatch Precipitation," *Chem. Eng. Sci.*, **50**, 1281 (1995).

Barresi, A. A., D. Marchisio, and G. Baldi, "On the Role of Micro- and Mesomixing in a Continuous Couette-Type Precipitator," *Chem. Eng. Sci.*, **54**, 2339 (1999).

Bromley, L. A., "Thermodynamic Properties of Strong Electrolytes in Aqueous Solutions," *AIChE J.*, **19**, 313 (1973).

Butkus, M. A., and D. Grasso, "Impact of Aqueous Electrolytes on Interfacial Energy," *J. Colloid Interface Sci.*, **200**, 172 (1998).

Camp, T. R., and P. C. Stein, "Velocity Gradients and Internal Work in Fluid Motion," *J. Boston Soc. Civil Eng.*, **30**, 219 (1943).

David, R., "General Rules for Prediction of the Intensity of Micromixing Effects on Precipitation," *Powder Technol.*, **121**, 2 (2001).

Eble, A., "Precipitation of Nanoscale Crystals with Particular Reference to Interfacial Energy," PhD Thesis, Technische Universität München, Germany (2000).

Felmy, A. R., D. Rai, and J. E. Amonette, "The Solubility of Barite and Celestite in Sodium Sulfate: Evaluation of Thermodynamic Data," *J. Solution Chem.*, **19**, 175 (1990).

Fuchs, N., "Über die Stabilität und Aufladung der Aerosole," *Z. Phys.*, **89**, 736 (1934).

Gmelin Handbook of Inorganic and Organometallic Chemistry Supplement, Barium, 8th Edition, Verlag Chemie, Weinheim, Germany (1960).

Heyer, C., "Production of Nano-sized Particles by Drowning-out Precipitation," PhD Thesis, Technische Universität München, Germany (2000).

Hunter, R. J., *Foundations of Colloid Science*, Vol. 1, Oxford University Press, Oxford, UK 1(986).

Israelachvili, J., *Intermolecular and Surface Forces*, 2nd Edition, Academic Press, London (1991).

Jiang, C., "Solubility and Solubility Constants of Barium Sulfate in Aqueous Sodium Sulfate Solutions between 0 and 80°C," *J. Solution Chem.*, **25**, 105 (1996).

Judat, B., and M. Kind, "Effects of Mixing on the Precipitation of Barium Sulfate in a Taylor–Couette Reactor with Axial Flow," Proc. of the 15th Int. Symp. on Industrial Crystallization, Sorrent, Italy, Sep. 15–18, Vol. 1, pp. 281–286 (2002).

Kruis, F. E., and K. A. Kusters, "The Collision Rate of Particles in Turbulent Flow," *Chem. Eng. Commun.*, **158**, 201 (1997).

Marchisio, D. L., A. A. Barresi, and M. Garbero, "Nucleation, Growth and Agglomeration in Barium Sulfate Turbulent Precipitation," *AIChE J.*, **48**, 2039 (2002).

Melis, S., M. Verduyn, G. Storti, M. Morbidelli, and J. Baldyga, "Effect of Fluid Motion on the Aggregation of Small Particles Subject to Interaction Forces," *AIChE J.*, **45**, 1383 (1999).

Mersmann, A., "Calculation of Interfacial Tensions," *J. Crystal Growth*, **102**, 841 (1990).

Mersmann, A., *Crystallization Technology Handbook*, 2nd Edition, Marcel Dekker, New York (2000).

Mersmann, A., K. Bartosch, B. Braun, A. Eble, and C. Heyer, "Möglichkeiten einer vorhersagenden Abschätzung der Kristallisationskinetik," *Chem.-Ing.-Tech.*, **72**, 17 (2000).

Monnin, C., "A Thermodynamic Model for the Solubility of Barite and Celestite in Electrolyte Solutions and Seawater to 200°C and to 1 kbar," *Chem. Geol.*, **153**, 187 (1999).

Monnin, C., and C. Galinier, "The Solubility of Celestite and Barite in Electrolyte Solutions and Natural Waters at 25°C: A Thermodynamic Study," *Chem. Geol.*, **71**, 283 (1988).

Nielsen, A. E., and O. Söhnel, "Interfacial Tensions in Electrolyte Crystal-Aqueous Solution, from Nucleation Data," *J. Crystal Growth*, **11**, 233 (1971).

Phillips, R., S. Rohani, and J. Baldyga, "Micromixing in a Single-Feed Semi-Batch Precipitation Process," *AIChE J.*, **45**, 82 (1999).

Saffman, P. G., and J. S. Turner, "On the Collision of Drops in Turbulent Clouds," *J. Fluid Mech.*, **1**, 16 (1956).

Schlomach, J., M. Kind, S. Schulze, R. Maus, and M. Freyer, "Experiments on the Formation and Aggregation of Nano-sized Precipitates under Shear Stress," Proc. of the 15th Int. Symp. on Industrial Crystallization, Sorrent, Italy, Sep. 15–18, Vol. 1. pp. 281–286 (2002).

Schubert, H., "Keimbildung bei der Kristallisation schwerlöslicher Feststoffe," PhD Thesis, Technische Universität München, Germany (1998).
Schwarzer, H.-C., and W. Peukert, "Experimental Investigation into the Influence of Mixing on Nanoparticle Precipitation," *Chem. Eng. Technol.*, **25**, 657 (2002).
Schwarzer, H.-C., and W. Peukert, "Tailoring Particle Size through Nanoparticle Precipitation," *Chem. Eng. Commun.*, **191**, 580 (2004).
Schwarzer, H.-C., and W. Peukert, "Prediction of Aggregation Kinetics Based on Surface Properties of Nanoparticles," *Chem. Eng. Sci.*, in press (2005).
Sugimoto, T., "A New Approach to Interfacial Energy: 1. Formulation of Interfacial Energy," *J. Colloid Interface Sci.*, **181**, 259 (1996).
Sugimoto, T., "A New Approach to Interfacial Energy: 2. Interfacial Energies of Different Interfaces under the Influence of Adsorption," *J. Phys. Chem. B*, **103**, 3593 (1999).
Telib, H., A. Iollo, and M. Manhart, "Analysis and Low Order Modeling of the Inhomogeneous Transitional Flow Inside a T-Mixer," *Phys. Fluids*, **16**, 2717 (2004).
Torbacke, M., and A. C. Rasmuson, "Influence of Different Scales of Mixing in Reaction Crystallization," *Chem. Eng. Sci.*, **56**, 2459 (2001).
von Smoluchowski, M., "Versuch einer mathematischen Theorie der Koagulationskinetik kolloidaler Lösungen," *Z. Phys. Chem.*, **92**, 129 (1917).

Manuscript received Sep. 22, 2003, and revision received Apr. 8, 2004.